Sun *et al. Biology Direct* (2025) 20:5
https://doi.org/10.1186/s13062-025-00596-0

Biology Direct

RESEARCH Open Access

OSBPL3 modulates the immunosuppressive microenvironment and predicts therapeutic outcomes in pancreatic cancer

Qihui Sun[1†], Xiaoqi Zhu[1,2†], Qi Zou[1,2†], Yang Chen[1], Tingting Wen[1], Tingting Jiang[1], Xiaojia Li[1], Fang Wei[1,2*], Keping Xie[1*] and Jia Liu[3*]

Abstract

Background Pancreatic cancer is characterized by a complex tumor microenvironment that hinders effective immunotherapy. Identifying key factors that regulate the immunosuppressive landscape is crucial for improving treatment strategies.

Methods We constructed a prognostic and risk assessment model for pancreatic cancer using 101 machine learning algorithms, identifying OSBPL3 as a key gene associated with disease progression and prognosis. We integrated multi-dataset analyses, single-cell transcriptomic data, and functional experiments to explore the role of OSBPL3 in pancreatic cancer.

Results Our risk prediction model, developed using machine learning algorithms, demonstrated high predictive accuracy across multiple datasets. Notably, the "rf" algorithm model showed an AUC of 1 in the training set and AUCs of 0.887 and 0.977 in two validation datasets. Ridge regression analysis identified OSBPL3 as a core prognostic feature gene. High OSBPL3 expression in pancreatic cancer samples was associated with immunosuppressive characteristics, including reduced CD8 + T cell infiltration and increased immunosuppressive cell populations such as Treg cells and M2 macrophages. Transcriptomic sequencing following OSBPL3 knockdown revealed enrichment of immune-related pathways, suggesting OSBPL3's influence on the immune microenvironment. Single-cell analyses further confirmed OSBPL3's role in shaping the immunosuppressive landscape by modulating Treg cells and M2 macrophages. Additionally, OSBPL3 expression was linked to resistance to immunotherapy, with high OSBPL3 expression associated with lower Immunophenoscore (IPS) scores, indicating poor responsiveness to immunotherapy.

Conclusions Our study reveals OSBPL3 as a critical regulator of the immunosuppressive microenvironment in pancreatic cancer and a potential therapeutic target. Targeting OSBPL3 may enhance the efficacy of immunotherapy

†Qihui Sun, Xiaoqi Zhu and Qi Zou contributed equally to this work.

*Correspondence:
Fang Wei
eyfangwei@scut.edu.cn
Keping Xie
scutmedicine@scut.edu.cn
Jia Liu
mcliujia@scut.edu.cn

Full list of author information is available at the end of the article

and improve patient outcomes. Further research is warranted to explore OSBPL3 as a biomarker for predicting immunotherapy response and as a potential therapeutic target in combination with anti-PD1 therapy.

Introduction

Pancreatic cancer is one of the most aggressive malignancies, with pancreatic ductal adenocarcinoma (PDAC) accounting for over 90% of cases [1, 2]. Currently, the incidence of pancreatic cancer has surpassed that of breast cancer and is projected to overtake colorectal cancer by 2040, becoming the second leading cause of cancer-related deaths after lung cancer [3]. Due to the extremely low survival rates, the incidence and mortality of pancreatic cancer are nearly equivalent [4, 5]. The tumor microenvironment (TME), comprising stromal cells, blood vessels, immune cells, signaling molecules, and the extracellular matrix, plays a pivotal role in the development and progression of PDAC [6]. The dense fibrotic stroma in pancreatic cancer acts as a barrier that disrupts angiogenesis, leading to impaired blood perfusion and hypoxia [7]. Additionally, activated fibroblasts within the pancreatic stroma acquire a myofibroblast phenotype, promoting dense fibrosis by secreting laminin, fibronectin, and collagen [8]. This dense fibrotic microenvironment restricts the pro-angiogenic capacity of angiogenic factors, while the poor vascularization can trigger autophagy in tumor cells. Immune cells are central to the TME in PDAC. Pancreatic cancer is well known for recruiting myeloid cells and fibroblasts with immunosuppressive and tumor-promoting characteristics. Regulatory T cells (Tregs), tumor-associated macrophages (TAMs), and myeloid-derived suppressor cells (MDSCs) collectively establish an immunosuppressive microenvironment [9]. These inhibitory cell populations suppress or eliminate the activity of anti-tumor effector cells. Research has shown that macrophages can secrete cytidine deaminase to reduce apoptosis [10]. Although immunotherapy has revolutionized cancer treatment and shown significant clinical benefits in hematological malignancies and some solid tumors, pancreatic cancer patients rarely respond effectively due to the complex immunosuppressive microenvironment [11]. Therefore, targeting key genes that promote the formation of the immunosuppressive microenvironment may activate effector T cells, enhance the efficacy of immunotherapy, and bring new hope to pancreatic cancer patients.

OSBPL3, a member of the oxysterol-binding protein-related protein (ORP) family, comprises 23 exons and encodes a predicted protein of 887 amino acids with a carboxy-terminal ORD domain and an amino-terminal PH domain [12]. Under physiological conditions, OSBPL3 primarily mediates cellular adhesion, lipid transport, actin cytoskeleton regulation, and signal transduction between the endoplasmic reticulum and plasma membrane [13]. The expression of OSBPL3 is cell- and tissue-specific, being highly expressed in organs such as the kidney, bladder, bone marrow, and endocrine system, as well as in immune cells, including macrophages, T cells, and B cells [14, 15].

As a key component of the sterol synthesis pathway, OSBPL3 may support pancreatic cancer cell growth, proliferation, and division by participating in lipid metabolism reprogramming and activating various oncogenic pathways [16, 17]. Moreover, OSBPL3 is likely involved in remodeling the tumor microenvironment, facilitating immune evasion, and influencing the efficacy of immunotherapy [18]. In this study, we employed immune infiltration analysis and cell-cell communication analysis to investigate whether OSBPL3 mediates alterations in the immune microenvironment and to explore its potential role in modulating the effectiveness of immunotherapy, focusing on the critical cell-cell signaling pathways involved.

Methods and materials

Data acquisition

The transcriptome sequencing of NC and OSBPL3-Si was conducted on PAAD cell line of CFPAC using Illumina Novaseq6000 by Gene Denovo Biotechnology Co. (Guangzhou, China). We obtained transcriptomic count data for pancreatic ductal adenocarcinoma (PDAC) and normal pancreatic tissues from the UCSC XENA database (https://xena.ucsc.edu/) (TCGA-PAAD and GTEx datasets) for subsequent differential expression analysis. The transcriptomic data were normalized using Transcripts Per Million (TPM) to account for gene expression across transcripts per kilobase per million mapped reads, facilitating further analyses. Additionally, we downloaded the corresponding clinical data, which included survival information, to perform survival analysis and construct predictive models. In total, we acquired 178 pancreatic tumor samples and 170 normal control samples. Upon re-evaluation of all pathology slides, 150 samples were confirmed as PDAC and subsequently included in downstream analyses.

Furthermore, expression profile data from pancreatic cancer transcriptomic datasets—GSE16515, GSE62452, GSE71729, and GSE32676—were downloaded from the GEO database (https://www.ncbi.nlm.nih.gov/geo/). We also obtained single-cell transcriptomic datasets GSE155698, GSE141017, and GSE78220, which include multiple pancreatic cancer samples, to enable more in-depth analyses. We also utilized two spatial transcriptomic datasets, GSE111672 and GSE203612, to

investigate the spatial distribution of different immune cell populations. Details of each dataset and the respective groupings are provided in the following table (Table 1).

Data processing

The transcriptome data matrix was downloaded and processed based on the sequencing platform. Seurat objects were created using the "Read10X" and "CreateSeuratObject" functions from the Seurat package. Filtering criteria included nFeature_RNA > 200, nFeature_RNA < 6000, and percent.mt < 10 to ensure high-quality data. To mitigate technical biases introduced during the sequencing process, the data was normalized using the "NormalizeData" function from the Seurat package. After normalization, "FindVariableFeatures" was employed to identify the top 2000 highly variable genes (HVGs) based on their contribution to data variability for subsequent analyses. Principal component analysis (PCA) was performed using the "RunPCA" function for linear dimensionality reduction. Next, clustering was conducted using the "FindNeighbors" and "FindClusters" functions, which apply a K-Nearest Neighbor (KNN) algorithm based on manifold learning. Finally, the clustering results were visualized using t-distributed Stochastic Neighbor Embedding (t-SNE) and Uniform Manifold Approximation and Projection (UMAP), two widely used nonlinear dimensionality reduction algorithms. These visualization approaches provided a clear representation of the clustering patterns and data structure.

Pancreatic cancer survival prediction and risk assessment models

To construct survival prediction and risk assessment models for pancreatic cancer, transcriptome data from dataset GSE16515, comprising 16 normal control samples and 36 pancreatic cancer tumor samples, was analyzed for differential expression. A total of 189 upregulated genes in tumor tissues were identified as the candidate gene set for model construction. Dataset GSE16515 was used as the training set, while datasets GSE62452 and TCGA-GTEx served as validation sets for building and validating the risk assessment models. For survival prediction models, datasets with survival data, including GSE62452 and GSE71729, were utilized.

Using the "Mime" package, the "ML.Dev.Pred.Category.Sig" function was applied to combine the training and validation datasets with the 189 candidate genes. This enabled the construction of risk models using seven machine learning algorithms, including "rt" and "adaboost". The "roc_vis_category" function was employed to generate ROC curves, visualizing the Area Under the Curve (AUC) values for each model across the training and validation datasets.

For survival prediction, the "ML.Dev.Prog.Sig" function integrated the datasets and candidate genes to construct prognostic models using ten machine learning algorithms. The "cindex_dis_all" function visualized the C-indices of these models, while the "survplot" and "all.auc.1y" functions analyzed survival differences between high- and low-risk groups and predicted 1-year survival outcomes.

To identify prognostically relevant features, the "ML.Corefeature.Prog.Screen" function selected features through eight machine learning algorithms. The "core_feature_select" function identified the intersection of these features, and the "core_feature_rank" function ranked the top 20 key genes contributing to pancreatic cancer prognosis.

Table 1 Datasets

Database	Dataset	Species	GPL	Number(*n*)
TCGA	TCGA-GTEx	human		Normal: 170 PDAC: 150
GEO	GSE16515	human	GPL570	Normal: 16 PDAC: 36
GEO	GSE62452	human	GPL6244	Normal: 69 PDAC: 69
GEO	GSE71729	human	GPL20769	Normal: 46 PDAC: 145
GEO	GSE32676	human	GPL198	Normal: 7 PDAC: 42
GEO	GSE155698	human		Normal: 7 PDAC: 42
GEO	GSE141017	mouse		CTRL-tumor:7
GEO	GSE205049	human		Normal: 9 PDAC: 9

Weighted gene co-expression network analysis (WGCNA)

Single-cell transcriptome data from a KC mouse model was preprocessed using the Seurat package, including imputation of missing values, batch effect correction, and outlier removal. To manage the large number of cells in single-cell sequencing data, pseudocells were generated to reduce cell count. Genes were further filtered based on expression levels to meet analysis requirements.

WGCNA was conducted by setting correlation analysis methods and Topological Overlap Matrix (TOM) type parameters. The "pickSoftThreshold" function determined the soft threshold, and the "blockwiseModules" function was applied to construct a gene co-expression network using the one-step method. The "plotDendroAndColors" function produced a clustering dendrogram, and the "plotEigengeneNetworks" function generated a correlation heatmap of the modules.

Subsequently, the Mfuzz package was used to analyze the cell trajectory trends within each module. Genes in selected modules were identified based on correlation analysis, and their expression levels were visualized for further interpretation.

Overexpression plasmid and siRNA transfections

Small interfering RNA (siRNAs) were synthesized from GenePharma (Shanghai, China) to target OSBPL3 (5'-GCAAGAAGAUCUGUGUCAUTT-3'), or negative control

(5'-UUCUCCGAAGGUGUCACGUTT – 3'). Overexprssion plasmids for OSBPL3 both human and mouse were purchased from GenScript (HK, China). Lipofectamine 3000 (Invitrogen; Thermo Fisher Scientific, Inc.) and Opti-MEM Medium (Gibco; Thermo Fisher Scientific, Inc.) were applied to transfect siRNAs or overexprssion plasmid according to the manufacturer's protocol. The transfected efficiency was validated by qRT-PCR (48 h after transfection) and western blot (72 h after transfection).

Mouse tumorigenesis assay

Panc02 mouse pancreatic cancer cells were divided into two groups. Following transfection with the PC3.1 vector and the OSBPL3 overexpression plasmid, the cell suspensions were mixed with Matrigel in equal proportions and injected into mice for tumorigenesis experiments. Tumor size measurements were initiated 7 days post-injection, and survival curves were plotted. Finally, tumor tissues were harvested, fixed in formalin, dehydrated stepwise, embedded in paraffin, sectioned, and subjected to immunofluorescence staining.

Immune infiltration analysis

To investigate the relationship between OSBPL3 expression and immune infiltration in pancreatic cancer, we utilized the R package "GSVA" and "IOBR" to predict scores for various immune cell types based on immune-related gene sets. This approach allowed us to assess the association between OSBPL3 expression and immune cell infiltration. Additionally, Spearman correlation analysis was employed to describe the relationship between OSBPL3 expression levels and the infiltration of specific immune cell populations.

Differential expression analysis and pathway enrichment analysis

To identify the differences in gene expression among various clusters, we employed the "FindAllMarkers" function to analyze the marker genes specific to each group. Heatmaps (generated using the "DoHeatmap" function), violin plots ("VlnPlot" function), and dimensionality reduction plots ("FeaturePlot" function) were utilized to visualize the differential expression of genes across clusters.

The R package "msigDB" was employed to access commonly used gene sets from the MSigDB database (http://www.gsea-msigdb.org/gsea). GSVA analysis was pe rformed using the "msigdbr" function.Gene Ontology (GO) and KEGG pathway enrichment analyses were conducted using the "enrichKEGG" and "enrichGO" functions from the "clusterProfiler" R package. Visualization of the results was facilitated through the "enrichplot" and "ggplot2" packages.

Slingshot pseudotime analysis

To delineate gene expression patterns and evolutionary trajectories during pancreatic cancer progression, the Slingshot algorithm was employed to construct cell differentiation lineage structures and infer pseudotemporal dynamics across different lineages.

After filtering genes, normalizing data, and performing dimensionality reduction via UMAP, the SingleCellExperiment package was used to convert Seurat objects into SingleCellExperiment objects. Cell coordinate matrices and cluster labels were input into the Slingshot package to identify global lineage structures via Minimum Spanning Tree (MST) and fit major curves.

The resulting differentiation trajectories and pseudotime inferences were projected onto the UMAP space, providing a comprehensive view of gene expression dynamics and evolutionary trajectories in distinct cell subpopulations.

Cellchat cell communication analysis

Cell communication analysis was performed using the CellChat package. The process began by creating a CellChat object from a Seurat object using the createCellChat function, with the group.by parameter defined for grouping.The constructed CellChat object was then analyzed to identify overexpressed genes using the identifyOverExpressedGenes function and overexpressed ligand-receptor pairs with the identifyOverExpressedInteractions function. The computeCommunProb function was applied to infer the cell interaction probabilities within the CellChat object, followed by the computeCommunProbPathway function to calculate the communication results for all ligand-receptor interactions across different signaling pathways. Finally, visualization of the cell communication results was carried out using the netVisual_circle, netVisual_aggregate, netVisual_bubble, and plotGeneExpression functions.

NicheNet-based cell-cell communication analysis

To investigate ligand-receptor interactions, species-specific datasets, including lr_network, ligand_target_matrix, and weighted_networks, were preloaded for subsequent analysis. Single-cell transcriptomic data preprocessed using the Seurat package were then imported.

The receiver cell population was defined as "ductal cell (high)." Using the nichenet_seuratobj_aggregate function, cell-cell communication was analyzed between all cell types as potential senders and "ductal cell (high)" as the receiver. The results were visualized through ligand Expression Bubble Plots, which depicted the expression levels of key ligands across sender cells and ligand-Target Interaction Heatmaps, which highlighted the reliability and strength of signaling interactions between ligands and their corresponding target genes.

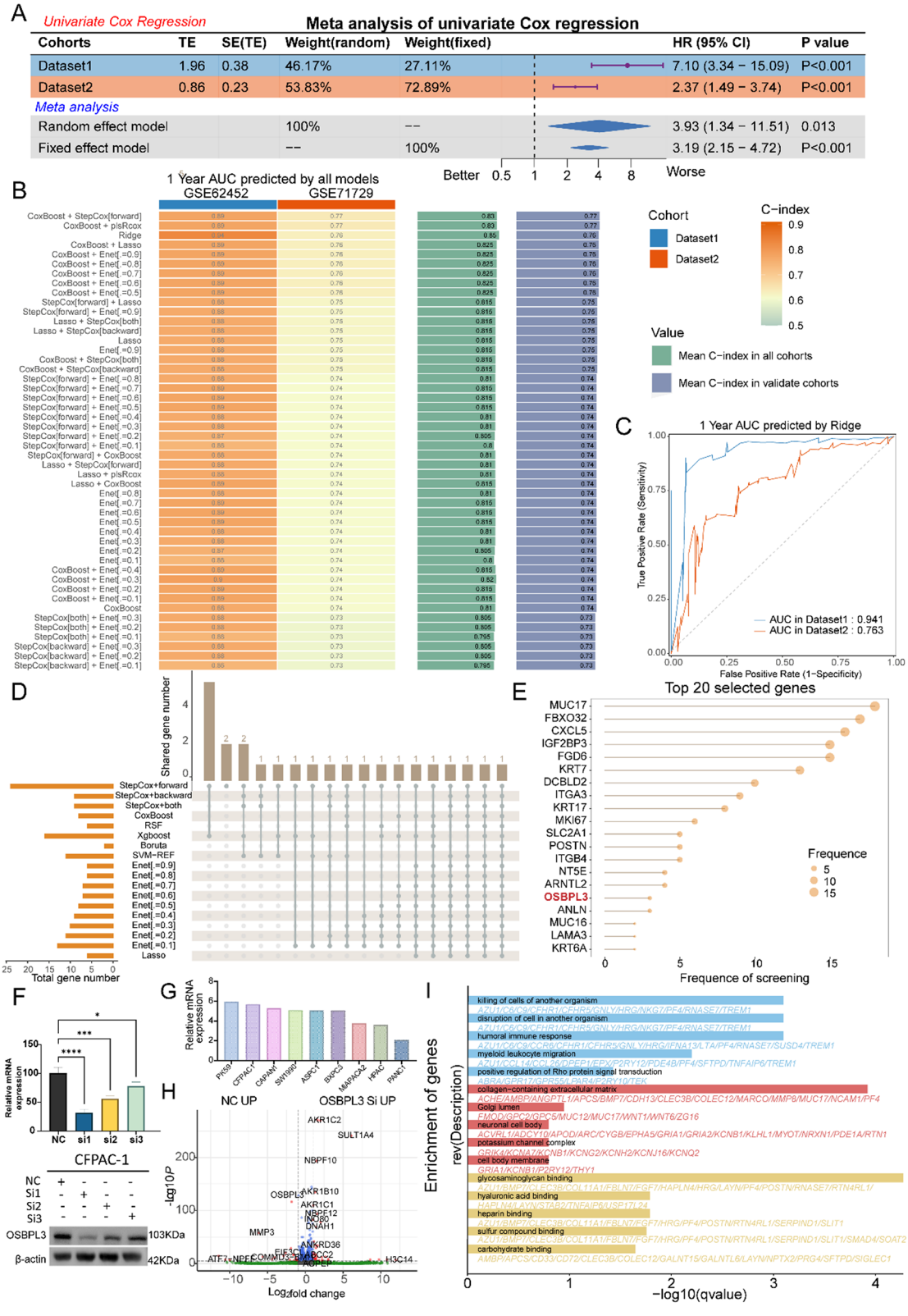

Fig. 1 (See legend on next page.)

(See figure on previous page.)

Fig. 1 OSBPL3 in Prognostic Prediction and Risk Assessment Model Construction for Pancreatic Cancer. (**A**) A forest plot illustrating the univariate regression analysis results of risk factor scores derived from the ridge regression model across different datasets. (**B**) A heatmap displaying the performance of 10 machine learning algorithm combinations in constructing 1-year survival prediction models for pancreatic cancer. The training dataset is geneset1 (GSE62452), and the validation dataset is geneset2 (GSE71729). The heatmap is ranked by the C-index values from the validation dataset, with colors representing the C-index scores.(**C**) Receiver operating characteristic (ROC) curves generated by the ridge regression model to evaluate the predictive performance for 1-year survival across different datasets. (**D**) Bar plots showing the integration of eight machine learning algorithms into 18 combinations to identify core prognostic feature genes. The left bar plot displays the number of core feature genes identified by each algorithm combination, while the top bar plot highlights the number of shared genes among different combinations. (**E**) A lollipop plot illustrating the frequency of core feature genes identified by different algorithm combinations, highlighting the top 20 genes with the highest frequencies. The length of the bars and the size of the circles represent the frequency of each gene. (**F**) qRT-PCR and Western blot analyses demonstrate the knockdown efficiency of three OSBPL3 siRNA sequences at the transcriptional and protein levels. (**G**) A bar chart illustrates the expression levels of OSBPL3 in commonly used pancreatic cancer cell lines from the CCLE database. (**H**) A volcano plot shows the differentially expressed genes between OSBPL3 knockdown and control groups in the CFPAC-1 pancreatic cancer cell line, based on transcriptomic sequencing. The threshold for differential expression was set to $|Log2FC| > 1$ and P-value < 0.05. Green dots represent genes that met the criteria for differential expression. Genes upregulated in the control group are shown on the left y-axis, while genes upregulated in the OSBPL3 knockdown group are shown on the right. (**I**) Pathway enrichment analysis of the differentially expressed genes in the OSBPL3 knockdown group

ScDist distance analysis

Following normalization of the Seurat object using the SCTransform function, dimensionality reduction and clustering analyses were performed. Subsequently, the scale.data and meta.data were extracted to construct a list. Using the scDist function, the fixed.effects parameter was set to group cells based on high or low OSBPL3 expression, while the clusters parameter was assigned to represent functional cell groupings. Distance scores between different cellular subpopulations and OSBPL3 expression groups were calculated. Visualization of these scores was performed with the DistPlot function. Finally, the distGenes function was applied to evaluate the importance of genes between groups.

Data statistics and visualization

All statistical analyses were performed using R (version 4.1.2) and GraphPad PRISM software (version 9.3.0). For differential expression analysis between groups of cells, a two-sided Wilcoxon rank-sum test with Bonferroni FDR correction was used. All graph constructions in this study were carried out by using R package software. To determine statistical differences in different groups, we use the Wilcox test. The statistical significance of differences was determined using the log-rank test. $p < 0.05$ was defined as statistically significant.

Results

OSBPL3 involvement in pancreatic cancer risk assessment and prognostic prediction model construction

We constructed a pancreatic cancer prognostic and risk assessment model based on a combination of 101 machine learning algorithms, and identified key prognostic genes to more accurately predict pancreatic cancer risk and overall survival (Figure S1A). Initially, we selected 189 genes upregulated in tumor tissues from the GSE16515 dataset as a gene set. The GSE62452 pancreatic cancer dataset was used as the training set, while the GSE71729 and TCGA-PAAD datasets served as validation sets (Dataset1 and Dataset2). Using seven machine learning algorithms, we developed a risk prediction model for pancreatic cancer. The results indicated that models constructed with five algorithms, including "rf," "svmRadiaWeights," and "adaboost," achieved good predictive performance across all three datasets (AUC > 0.7). Additionally, models from all seven algorithms exhibited AUC values exceeding 0.9 in at least two datasets (Figure S1B). Notably, the model constructed using the "rf" algorithm showed an AUC of 1 in the training set, an AUC of 0.887 in Dataset1, and an AUC of 0.977 in Dataset2 (Figure S1B and S1C).

Subsequently, we used the aforementioned gene set to select independent prognostic risk factors for pancreatic cancer and constructed an optimal prognostic prediction model. As shown in Figure S1D, models constructed with various machine learning algorithms demonstrated good predictive performance. Among these, Ridge regression analysis yielded the highest C-index in both the training and validation sets (GSE62452 dataset: 0.81; GSE71729 dataset: 0.63). For one-year survival prediction, Ridge regression analysis showed an AUC of 0.941 in the GSE62452 dataset and an AUC of 0.763 in the GSE71729 dataset, indicating high predictive efficacy (Fig. 1A and B). Univariate Cox regression analysis of the models constructed using Ridge regression in both the training and validation sets revealed that they were independent risk predictors in both datasets (HRDataset1 = 7.10, HRDataset2 = 2.37) (Fig. 1A).

However, in the one-year survival prediction model, Ridge regression did not provide the optimal predictive performance in the training set (Fig. 1B). To further improve predictive efficacy, we used a combined CoxBoost and StepCox algorithm to construct the model. The C-index was 0.89 in the GSE62452 training set and 0.77 in the validation set (Fig. 1C). After dividing all samples into high and low-risk groups based on the risk factor scores derived from both models, survival analysis showed that patients in the high-risk group had significantly poorer

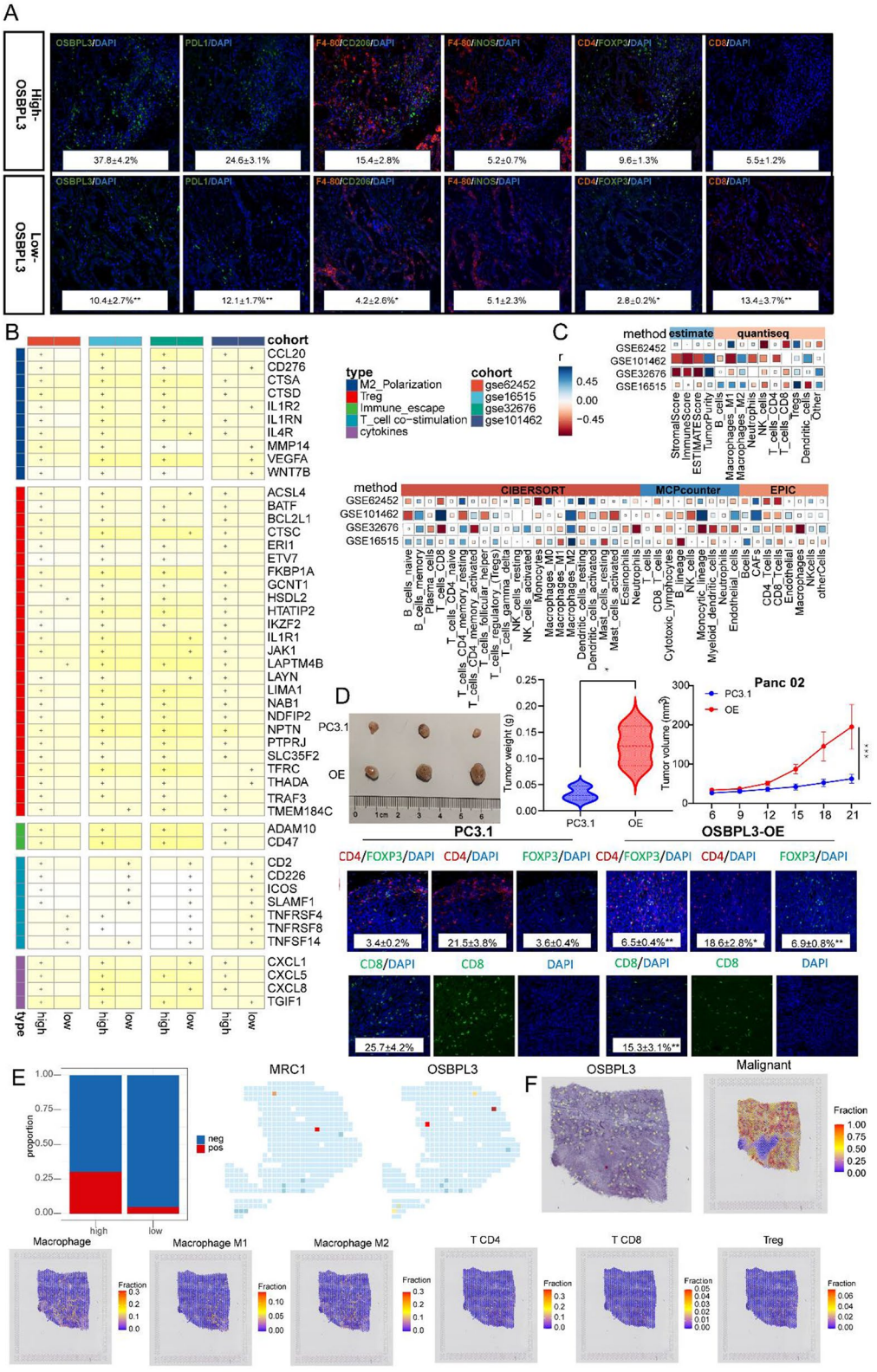

Fig. 2 (See legend on next page.)

(See figure on previous page.)

Fig. 2 Immune Cell Infiltration in Pancreatic Cancer Samples with High OSBPL3 Expression. (**A**) Representative immunofluorescence co-staining images of human pancreatic cancer samples in the high OSBPL3 expression group (High-OSBPL3) and the low OSBPL3 expression group (Low-OSBPL3), magnification: 20X. (**B**) Heatmap showing the expression of genes associated with M2 macrophage polarization and regulatory T cells (Tregs) in high and low OSBPL3 expression samples across the GSE62452, GSE16515, GSE32676, and GSE101462 datasets. Colors represent gene expression levels, and "+" indicates the high-expression group. (**C**) Correlation between OSBPL3 expression and immune cell infiltration predicted by algorithms such as ESTIMATE and EPIC across various pancreatic cancer datasets. Rows represent different datasets, and colors indicate the strength and direction of the correlation. (**D**) Subcutaneous tumor images, tumor weight and growth curve statistics, and representative immunofluorescence co-staining images of T-cell marker genes following OSBPL3 overexpression in B6/C57 mice. Magnification: 20X. (**E**) Expression distribution of OSBPL3 and the macrophage marker gene MRC1 in the pancreatic cancer spatial transcriptomics dataset GSE111672. The bar chart on the left shows the proportion of MRC1-positive cells in areas with high and low OSBPL3 expression. (**F**) Expression of OSBPL3 in the pancreatic cancer spatial transcriptomics dataset GSM6177618 and the tumor and immune cell expression distribution derived from immune cell deconvolution analysis based on "SpaCET"

prognosis (CoxBoost + StepCox (forward): *P*-value-Dataset1 < 0.001, *P*-value-Dataset2 < 0.001; Ridge: *P*-value-Dataset1 < 0.001, *P*-value-Dataset2 < 0.001), further demonstrating the robustness of the predictive models (Figure S2F).

After constructing both the pancreatic cancer risk prediction model and prognostic prediction model, we selected core prognostic features using 8 machine learning algorithms. As shown in Fig. 1D and 18 algorithm combinations were created by integrating the 8 machine learning algorithms, each of which identified a distinct set of prognostic core feature genes. Based on the frequency of appearance of these core feature genes, the top 20 genes were selected as candidate genes related to pancreatic cancer risk and prognosis (Fig. 1D and E).

Subsequently, we analyzed the single-cell transcriptomic data (GSE141017) from the KC mouse model (*Pdx1-Cre; Kras*$^{LSL-G12D/+}$) at various stages of disease progression using WGCNA. Two gene modules, blue (MEblue: $R = 0.87$, $P = 3e\text{-}112$) and brown (MEbrown: $R = 0.8$, $P = 1e\text{-}84$), showed the strongest correlation with disease progression (Figure S2A-C). MFUZZ time-course analysis revealed that genes within the blue and brown modules exhibited an increase in expression over time (Figure S2D). Based on these findings, we performed a combined analysis of the genes in the blue and brown modules from WGCNA with the 20 genes identified through the pancreatic cancer risk prediction model. The intersection of these two sets revealed a key gene, OSBPL3 (Figure S2E), suggesting that OSBPL3 may play an important role in the initiation and progression of pancreatic cancer.

High expression of OSBPL3 in pancreatic cancer samples exhibits immunosuppressive characteristics

The pancreatic cancer cell line CFPAC-1, exhibiting high OSBPL3 expression, was selected for OSBPL3 knockdown experiments. After successful knockdown, transcriptomic sequencing analysis was performed to explore the downstream molecular changes (Fig. 1F and G). Transcriptomic sequencing was performed on the CFPAC-1 pancreatic cancer cell line after knockdown of OSBPL3. The results revealed that several immune-related pathways, including myeloid leukocyte migration, were significantly enriched in the knockdown group (Fig. 1H and I). These findings suggested that OSBPL3 may influence the immune microenvironment, thereby contributing to the development and poor prognosis of pancreatic cancer.

We performed multiplex immunofluorescence analysis on multiple pancreatic cancer tissue samples, which revealed that the high-expression OSBPL3 group exhibited lower infiltration of $CD8^+$ T cells ($CD8^+$) but higher infiltration of immunosuppressive cells, including Treg cells ($CD4^+$ $FOXP3^+$) and M2 macrophages ($F4\text{-}80^+$ $CD206^+$) (Fig. 2A). Expression analysis of M2 macrophage polarization and Treg-related marker genes across four pancreatic cancer transcriptomic datasets, including GSE62452, showed that genes associated with M2 macrophage polarization (e.g., CCL20 and CTSA), Treg-related genes (e.g., BATF and GCNT1), and immune evasion genes were highly expressed in the OSBPL3 high-expression group. In contrast, T cell co-stimulation genes were more highly expressed in the OSBPL3 low-expression group (Fig. 2B). Immunoinfiltration analysis further confirmed the immunosuppressive characteristics of OSBPL3 high-expression samples (Fig. 2C and Figure S3A-C).

To further validate these findings, we utilized an OSBPL3 overexpression mouse subcutaneous tumor model for immunofluorescence staining. Compared to the control group, the OSBPL3 overexpression group (OSBPL3-OE) showed a decrease in the expression of $CD8^+$ T cell ($25.7 \pm 4.2\%$ and $15.3 \pm 3.1\%$) and CD4 + T cell ($21.5 \pm 3.8\%$ and $18.6 \pm 2.8\%$) markers, while the expression of Treg cell markers ($3.4 \pm 0.2\%$ and $6.5 \pm 0.4\%$)was increased(Fig. 2D). In the spatial transcriptomic dataset GSE111672, the high-expression regions of OSBPL3 also showed co-localization with the M2 macrophage marker gene MRC1 (Fig. 2F). Cluster and deconvolution analysis of the spatial transcriptomic dataset GSE203612 revealed that OSBPL3 is highly expressed in the pancreatic cancer region and co-localizes with malignant cancer cells. Additionally, OSBPL3 exhibited co-localization with macrophages, particularly M2 macrophages (Fig. 2F).

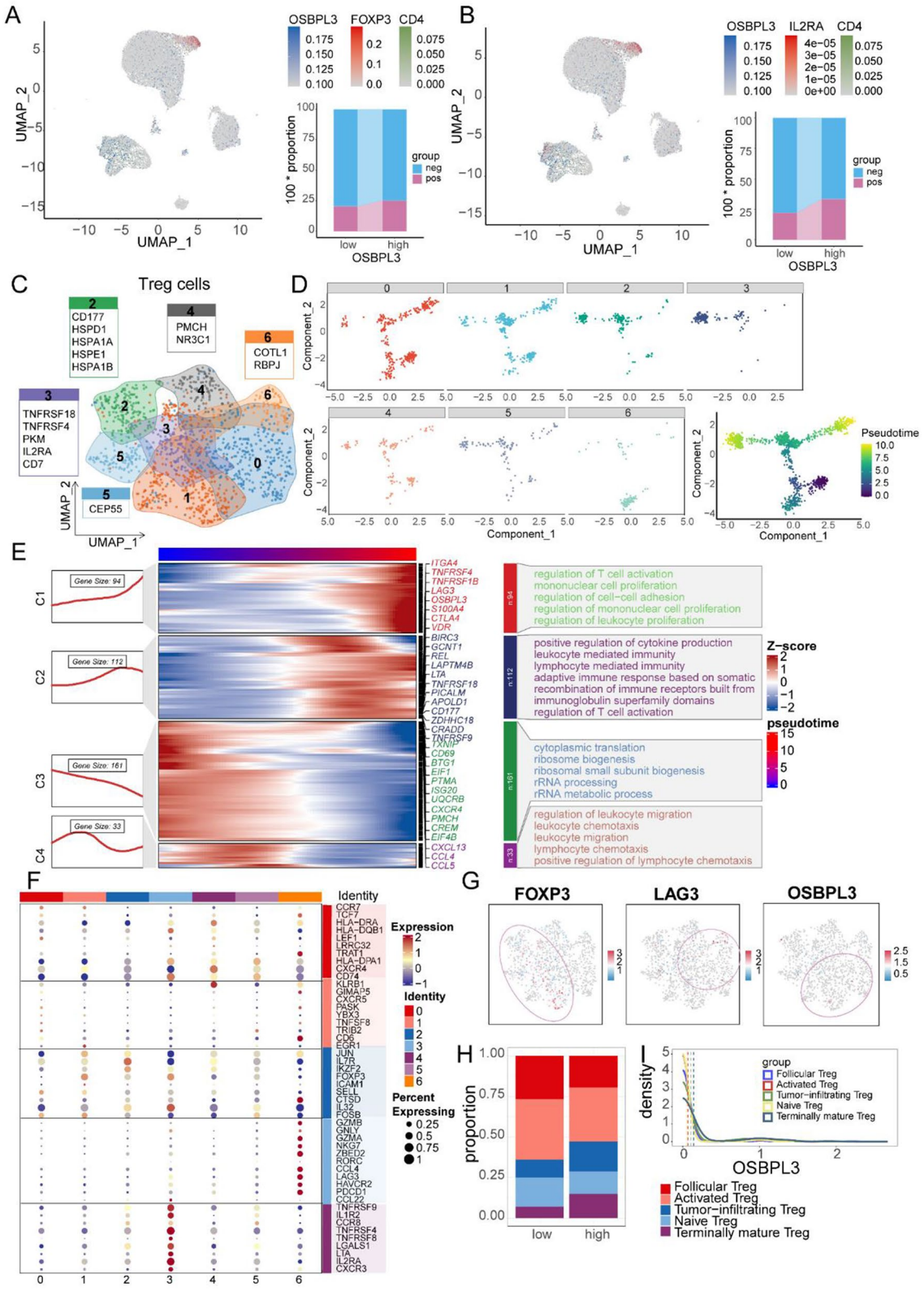

Fig. 3 (See legend on next page.)

(See figure on previous page.)

Fig. 3 Higher Tumor-Associated Treg Cell Infiltration in Pancreatic Cancer Samples with High OSBPL3. (**A**) Expression Proportion of FOXP3 and CD4 co-expressing cells in pancreatic cancer samples and their relative abundance in high (High-OSBPL3) and low (Low-OSBPL3) OSBPL3 expression groups. (**B**) Proportion of IL2RA and CD4 co-expressing cells in pancreatic cancer samples and their relative abundance in High-OSBPL3 and Low-OSBPL3 groups. (**C**) Dimensionality reduction and clustering of Treg cell subpopulations. Different colors represent distinct subclusters, and the differential expression genes for each subcluster are displayed. (**D**) Monocle trajectory analysis of Treg cell subpopulations, illustrating the inferred pseudotime progression across different subclusters. (**E**) Heatmap showing gene sets and their enriched pathways identified through pseudotime analysis across all Treg cell subpopulations. (**F**) Bubble plot depicting the expression of Treg cell marker genes across different Treg subpopulations. (**G**) Expression of FOXP3, LAG3, and OSBPL3 in Treg cells. (**H**) Proportions of different Treg subpopulations in High-OSBPL3 and Low-OSBPL3 groups. (**I**) Density plot showing the distribution of OSBPL3 expression across different Treg subpopulations

Analysis of various T cell subtypes further demonstrated a co-localization between OSBPL3 and Treg cells.

GSEA analysis of TCGA-PAAD pancreatic cancer samples revealed significant enrichment of immune deficiency-related pathways, including Immunodeficiency (NES = 1.35) and Impaired T Cell Function (NES = 1.46), in the OSBPL3 high-expression group. Pathways associated with macrophage proliferation and differentiation, as well as T cell immune negative regulation, also exhibited consistent trends (Figure S3D). These findings further confirm that high expression of OSBPL3 contributes to the establishment of an immunosuppressive microenvironment in pancreatic cancer.

Elevated expression of OSBPL3 in tumor-associated treg cells and M2 macrophages

To further elucidate the role of OSBPL3 in the tumor microenvironment, we leveraged the single-cell transcriptomic dataset GSE205049 to dissect immune landscapes in pancreatic cancer samples stratified by OSBPL3 expression. Following standardization, dimensionality reduction, clustering, and annotation, we identified 12 distinct cellular subpopulations (Figure S4A). Figures S4B-D illustrate the expression of marker genes, pathway enrichment profiles, and sample distribution across these subpopulations.

Subsequently, we focused our analysis on immune cells within the OSBPL3 high- and low-expression groups. The results (Figure S4E) revealed a significant reduction in CD8 + T cells and NKT cells in the OSBPL3 high-expression group, coupled with an enrichment of macrophages, dendritic cells, and Treg cells. These findings are consistent with prior immunofluorescence experiments and multi-dataset analyses. Differential gene expression analysis of immune cells highlighted upregulation of C1QB, APOE, and CD74 genes primarily implicated in immune evasion and the establishment of an immunosuppressive microenvironment—in the OSBPL3 high-expression group (Figure S4F).

To investigate T cell differentiation dynamics, we performed subclustering and pseudotime trajectory analysis using Slingshot, delineating the differentiation pathways of naïve T cells into mature T cell subsets (Figures S4G, S4I, S5A, and S5B). Functional annotation employing cytotoxicity and exhaustion markers demonstrated elevated cytotoxicity scores in NK and NKT cells, whereas Treg cells exhibited significantly higher exhaustion scores (Figures S4J and S5D). UMAP dimensionality reduction analysis further revealed high OSBPL3 expression in naïve T cells and Treg cells. Using the scDist algorithm, Treg cells emerged as the subpopulation most strongly associated with OSBPL3 expression differences (Figures S4K and S5C). This prompted us to delve deeper into the relationship between OSBPL3 expression and Treg cells.

Defining Treg cells through canonical markers such as CD4 and FOXP3 or IL2RA, we observed a marked increase in the proportion of double-positive Treg cells within the OSBPL3 high-expression group (Fig. 3A and B). Subsequent subclustering of Treg cells identified distinct subsets with differential gene expression profiles, which were utilized for functional annotation (Fig. 3C). Pseudotime analysis using Monocle revealed that subcluster 6 was predominantly composed of cells in the early differentiation phase, whereas subcluster 3 represented cells in the terminal differentiation phase (Fig. 3D). Clustering genes along pseudotime trajectories identified four gene modules, with OSBPL3, CTLA4, and LAG3 exhibiting progressive upregulation, indicating that OSBPL3 is predominantly expressed in terminally differentiated Treg cells (Fig. 3E). Functional annotation of Treg subclusters based on markers such as FOXP3 and LAG3 categorized these cells into Follicular Treg, Activated Treg, and Tumor-infiltrating Treg subsets (Fig. 3F and G). In OSBPL3 high-expression cells, the proportions of Tumor-infiltrating Treg and Terminally mature Treg subsets were significantly elevated, and these subsets displayed the highest OSBPL3 expression levels among all clusters (Fig. 3H and I).

To assess the implications of OSBPL3 in myeloid cells, we further subdivided myeloid populations into distinct subclusters, including those marked by SPP1 and C1QC, alongside eight additional subsets (Fig. 4A, Figure S5F and S5G). Notably, M2 macrophage marker-positive cells (CD68-MRC1 or CD68-CD163) were significantly more abundant in the OSBPL3 high-expression group (Fig. 4B). Monocle pseudotime analysis demonstrated that subcluster 0 comprised cells in the early and mid-differentiation stages, subcluster 2 in the mid-stage, subcluster 1 in the mid-to-late stage, and subcluster 3 in the terminal

differentiation stage. Cells from the OSBPL3 high-expression group predominantly exhibited an advanced differentiation state compared to their low-expression counterparts (Fig. 4C). Cluster enrichment analysis (Fig. 4D) revealed that genes upregulated in later differentiation phases were predominantly enriched in MHC-II-associated pathways.

Finally, we evaluated M2 polarization characteristics in myeloid cells stratified by OSBPL3 expression. As shown in Fig. 4E-G, myeloid cells with high OSBPL3 expression exhibited markedly elevated M2 polarization scores. Both OSBPL3 high-expression macrophage subclusters (Macrophage-SPP1 and Macrophage-C1QC) demonstrated prominent M2 polarization features. Moreover, knockdown of OSBPL3 in pancreatic cancer cells significantly reduced the expression of M2 polarization-related regulatory genes (Fig. 4H). These observations strongly suggest that pancreatic cancer cells modulate M2 macrophage polarization through OSBPL3 expression.

In summary, within the pancreatic tumor microenvironment, Treg cells progressively differentiate into tumor-associated and terminally mature Treg cells, while macrophages differentiate into subpopulations characterized by C1QC and APOE. OSBPL3 expression is increasingly upregulated during these differentiation processes, underscoring its potential role in shaping the immunosuppressive landscape of pancreatic cancer.

Pancreatic cancer cells induce immunosuppressive microenvironment formation via high expression of OSBPL3 and SPP1-mediated signals

The aforementioned results indicate a strong association between high OSBPL3 expression and tumor-associated Treg cells, as well as M2 macrophages characterized by APOE and C1QC expression. Knockdown or overexpression of OSBPL3 in pancreatic cancer cells significantly alters the expression of genes related to Treg cells and M2 macrophages, suggesting a pivotal role for OSBPL3 in shaping the immunosuppressive tumor microenvironment (TME).

To further investigate this mechanism, we utilized the single-cell transcriptomic dataset GSE155698, comprising 16 pancreatic cancer samples. Subclustering analysis revealed that OSBPL3 was highly expressed in tumor cells, whereas its expression was negligible in normal acinar cells (Fig. 5A). Defining a subset of tumor cells with high OSBPL3 expression, differential expression and enrichment analyses demonstrated significant upregulation of genes such as MMP14, which are implicated in pancreatic cancer progression and immune evasion. This subset was also enriched in oncogenic pathways, including TGF-β, MAPK, and WNT, while OSBPL3 low-expressing ductal cells were predominantly enriched in immune-related pathways, such as lymphocyte proliferation (Fig. 5B and C). Following OSBPL3 knockdown, the expression of WNT-related pathways, including the secretion of WNT ligands and canonical WNT target genes, was significantly reduced. Conversely, OSBPL3 overexpression in the PANC-1 cell line confirmed the association between high OSBPL3 expression and WNT pathway activation in pancreatic cancer (Fig. 5D-F). Previous studies have demonstrated that activation of the WNT signaling pathway promotes immune evasion and immunosuppression by regulating immune cell functions and modulating tumor microenvironment cytokines such as TGFB and CXCL12. Single-cell data analysis of pancreatic cancer revealed that genes encoding WNT ligands and Frizzled receptors were more highly expressed in the OSBPL3 high-expression group (Fig. 5G). Additionally, WNT pathway activation enhances the secretion of chemokines like CXCL12, contributing to the formation of an immunosuppressive microenvironment. In macrophages, T cells, and ductal cells, these chemokines were more abundantly expressed in OSBPL3 high-expression cells (Fig. 5H).

The results of CellChat analysis indicated that OSBPL3 high-expressing ductal cells exhibited significantly increased interactions with T cells, macrophages, endothelial cells, and fibroblasts compared to their low-expressing counterparts (Fig. 5I and S6A). Using NicheNet cell-cell communication analysis, we identified macrophage-derived SPP1 as a key ligand interacting with OSBPL3 high-expressing ductal cells (Fig. 5J). SPP1 is known to activate the WNT and MAPK/ERK signaling pathways, thereby promoting pancreatic cancer cell proliferation and survival [19, 20]. Moreover, OSBPL3 high-expressing ductal cells were found to produce significantly higher levels of SPP1 compared to their low-expressing counterparts, creating an autocrine feedback loop. These findings suggested that OSBPL3 facilitated SPP1 upregulation in tumor cells, promoting the recruitment of Treg cells and macrophages, ultimately fostering an immunosuppressive microenvironment.

Additionally, macrophages exhibit a positive feedback loop by upregulating SPP1, which in turn acts on tumor cells to activate oncogenic signaling pathways, further driving tumor proliferation and metastasis. Concurrently, T cells were shown to transmit inhibitory signals to OSBPL3 high-expressing ductal cells via TIGIT ligands.

Prediction of target genes for these ligands revealed that SPP1 likely regulates VCAN, whereas TIGIT may target SMAD3 (Figure S6B). VCAN is known to enhance pancreatic cancer cell proliferation and survival through activation of the PI3K/AKT pathway. SMAD3, a critical mediator of the TGF-β signaling pathway, is involved in pancreatic cancer invasion and metastasis. Notably, SMAD3 can synergize with the PI3K/AKT pathway to promote tumor cell proliferation. Both VCAN and

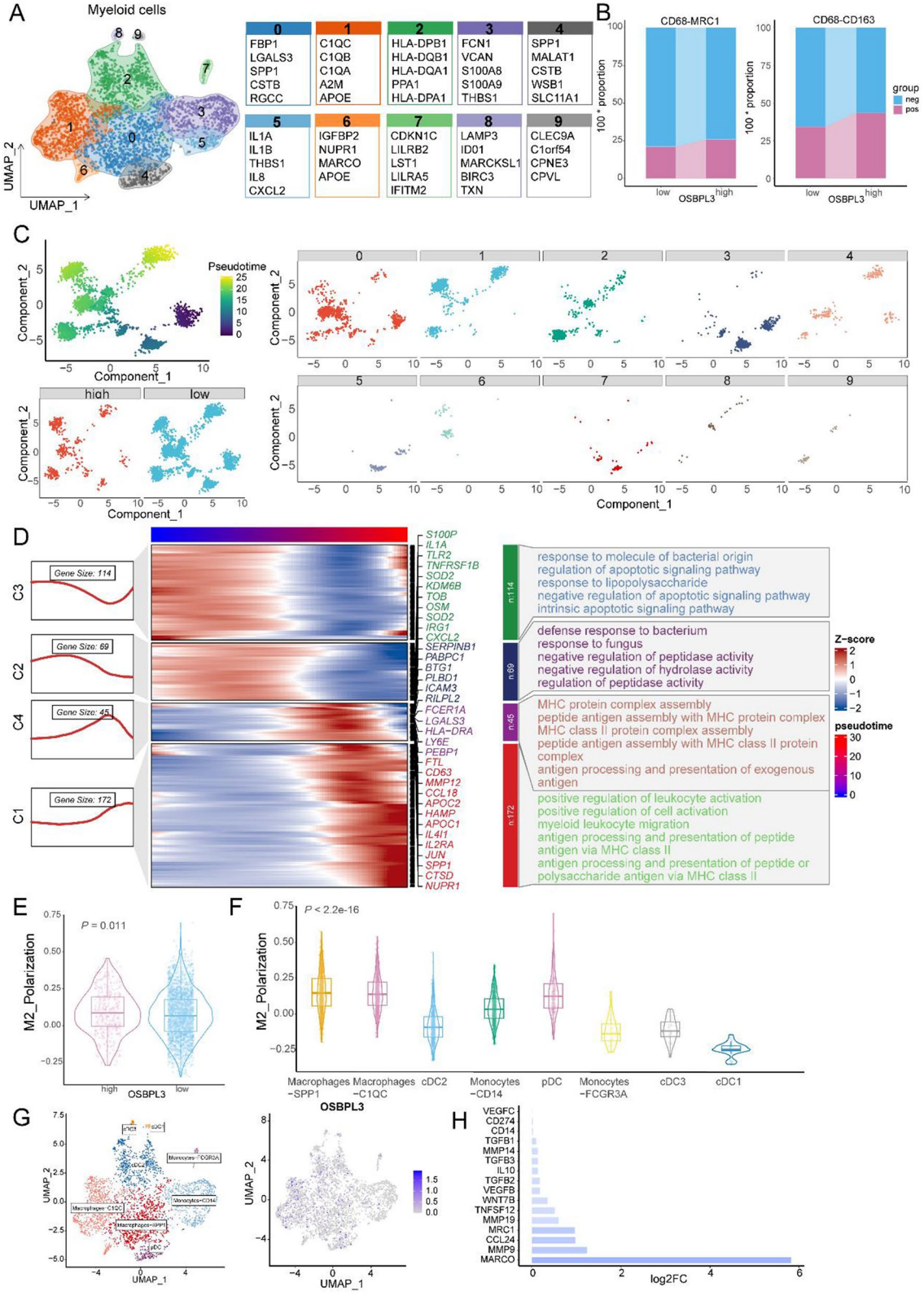

Fig. 4 (See legend on next page.)

(See figure on previous page.)

Fig. 4 Macrophages with High OSBPL3 Expression Exhibit a Stronger M2 Polarization Phenotype. (**A**) UMAP dimensionality reduction plot showing the distribution of myeloid cell subpopulations in pancreatic cancer samples, with differential marker genes identified for each subpopulation. (**B**) Bar plot displaying the proportion of CD68 and MRC1 or CD163 co-expressing cells in the high (High-OSBPL3) and low (Low-OSBPL3) OSBPL3 expression groups. (**C**) Monocle pseudotime analysis showing the trajectory of different cell subpopulations and OSBPL3 expression groups. (**D**) Heatmap illustrating key genes and enriched pathways identified from gene sets derived through monocle pseudotime analysis. (**E**) Violin plot comparing M2 macrophage polarization scores between High-OSBPL3 and Low-OSBPL3 groups. (**F**) Violin plot showing M2 macrophage polarization scores across different cell subpopulations. (**G**) UMAP plot displaying the proportions of functional subpopulations of myeloid cells and the expression of OSBPL3 within these subpopulations. (**H**) Scatter plot comparing the differential expression of M2 polarization-related genes between OSBPL3 knockdown and control groups. The x-axis represents Log2FC values for the two groups

SMAD3 contribute to immunosuppressive TME formation by inhibiting effector T cells, activating Treg cells, and recruiting immunosuppressive macrophages.

To validate these findings, we applied the CellChat package to further analyze cell-cell communication patterns identified via NicheNet. Ligand-receptor pair analysis highlighted an immunosuppressive TIGIT-PVR interaction between OSBPL3 high-expressing ductal cells and T cells, which was absent in OSBPL3 low-expressing cells (Figures S6C and S6D). Sequencing data from OSBPL3 knockdown in CFPAC-1 cells further confirmed a reduction in PVR expression upon OSBPL3 silencing (Figure S6E). Ligand analysis of ductal cells with high and low OSBPL3 expression revealed that OSBPL3-low-expressing ductal cells secreted significantly higher levels of the WNT pathway inhibitor DKK1, which is known to negatively regulate WNT signaling (Figure S6F). These findings suggest that high OSBPL3 expression may contribute to the formation of an immunosuppressive microenvironment in pancreatic cancer. This is likely mediated through the activation of pathways such as WNT and MAPK, which promote the secretion of immunosuppressive cytokines like TGFβ. This, in turn, facilitates the recruitment of macrophages and Treg cells, key immunosuppressive cell types. Furthermore, interactions involving ligand-receptor pairs, such as VCAN-SPP1 and PVR-TIGIT, may also play a role in reinforcing the immunosuppressive tumor microenvironment (Fig. 5K).

OSBPL3 is a potential therapeutic target in combination with anti-PD1 therapy

The potential impact of OSBPL3 on immunotherapy outcomes was further explored by evaluating its association with immune response-related gene signatures. Using the Immunophenoscore (IPS) framework, which incorporates key gene categories including MHC (antigen processing), EC (effector cells), CP (checkpoints), and SC (suppressor cells), we assessed the TCGA-PAAD pancreatic cancer cohort. As shown in Fig. 6A, samples with low OSBPL3 expression exhibited relatively higher IPS scores, while those with high OSBPL3 expression had lower IPS scores, indicating a potential correlation between OSBPL3 overexpression and poor responsiveness to immunotherapy. The mean IPS score for the OSBPL3 high-expression group was significantly lower than that of the low-expression group. Further statistical analysis of specific IPS components revealed that the MHC and EC scores were markedly reduced in the OSBPL3 high-expression group, reflecting diminished antigen presentation and effector cell activity. Conversely, the CP scores, indicative of checkpoints enrichment, were significantly higher in the OSBPL3 high-expression group (Fig. 6B and C). These findings suggested that OSBPL3 overexpression not only contributed to an immunosuppressive microenvironment but may have also underlain resistance to immunotherapy, potentially by impairing key immune functions, such as antigen presentation and effector cell activity, while enhancing suppressive mechanisms.

Given the low proportion of pancreatic cancer patients receiving immunotherapy, we sought to validate the role of OSBPL3 in pancreatic cancer immunotherapy. To this end, we utilized the melanoma dataset GSE78220 from the GEO database, which includes post-immunotherapy transcriptomic data. Using the scAB algorithm, we mapped the transcriptomic data and group information from GSE78220 onto single-cell data from pancreatic cancer, enabling us to predict the relationship between OSBPL3 expression and immunotherapy response. As shown in Fig. 6D, high OSBPL3 expression exhibited minimal overlap with scAB + cells (response cells), indicating that OSBPL3 may contribute to resistance to immunotherapy. We further analyzed the predictive role of OSBPL3 expression in immunotherapy response across other cancers. In the IMvigor210 mUC dataset and the GSE135222 lung cancer dataset, a lower proportion of immunotherapy responders was observed among OSBPL3-high-expressing samples. Conversely, samples responding to immunotherapy exhibited significantly lower OSBPL3 expression (Fig. 6E and F). Finally, in lung cancer samples, high OSBPL3 expression was associated with shorter progression-free survival (PFS) following immunotherapy (Fig. 6G). These results underscore the potential of OSBPL3 as a biomarker for predicting immunotherapy efficacy and outcomes.

Discussion

The complex pathogenesis of pancreatic cancer poses significant challenges in accurately assessing patients' risk and survival. Despite recent advances, the development

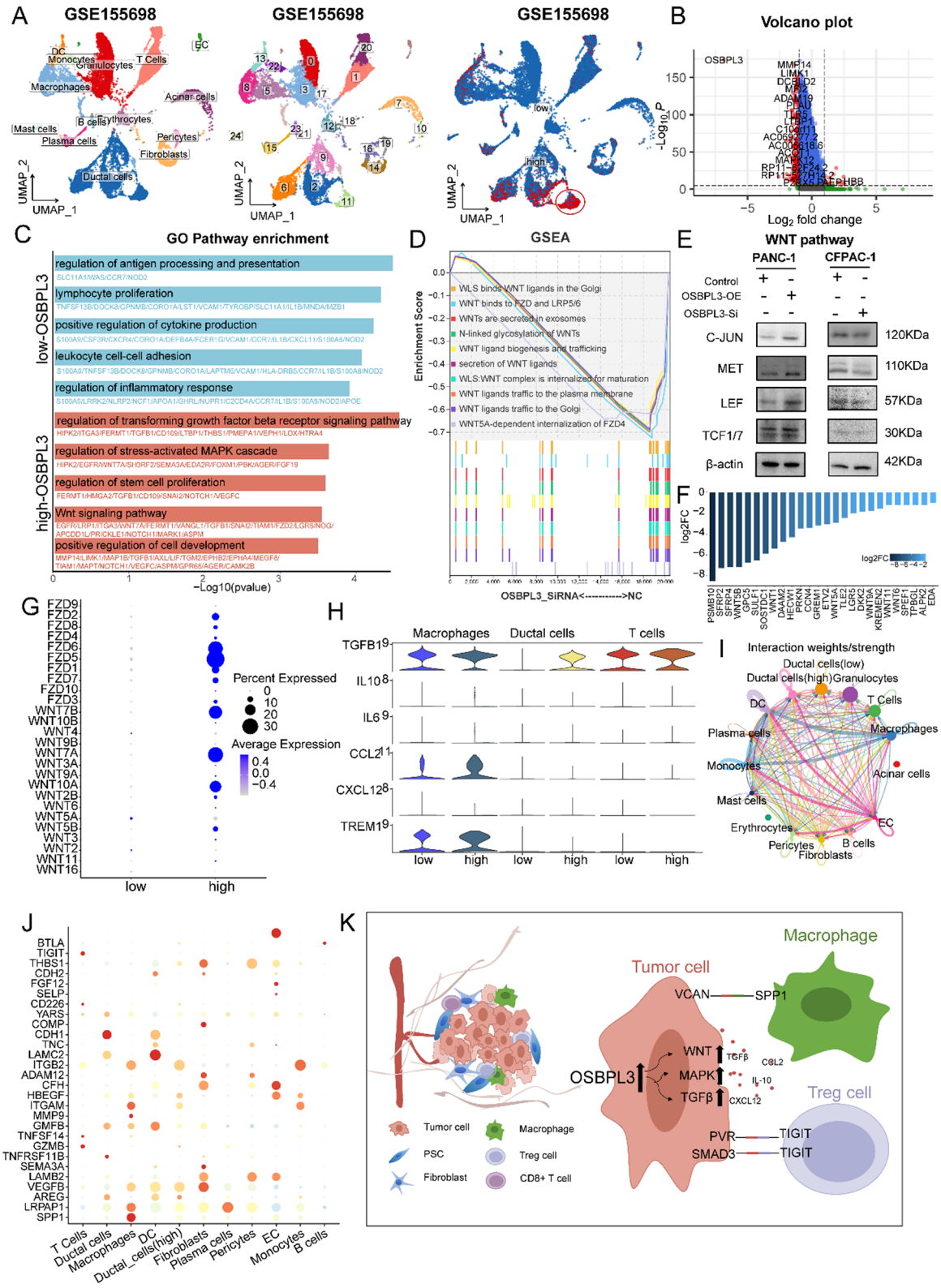

Fig. 5 (See legend on next page.)

(See figure on previous page.)

Fig. 5 Increased Inhibitory Cell-Cell Communication Between High OSBPL3 Expression Tumor and Immune Cells. (**A**) Dimensionality reduction and clustering of single-cell pancreatic cancer data from the GSE155698 dataset. (**B**) Volcano plot showing differentially expressed genes between OSBPL3 high-expression and low-expression ductal cell subpopulations. Genes upregulated in the low-expression group are on the left, while those upregulated in the high-expression group are on the right. (**C**) GO pathway enrichment analysis of differentially expressed genes in OSBPL3 high- and low-expression ductal cell subpopulations. Blue bars represent pathways enriched in the high-expression group, and red bars represent pathways enriched in the low-expression group. The x-axis indicates -Log10(p-value). (**D**) GSEA analysis of WNT-related pathways following OSBPL3 knockdown in the CFPAC-1 cell line. (**E**) Western blot analysis of WNT pathway gene expression after OSBPL3 knockdown or overexpression. (**F**) Expression changes of various WNT-related genes following OSBPL3 knockdown in the CFPAC-1 cell line. The x-axis represents gene names, and the y-axis shows the Log2FC values for differential expression between the knockdown and control groups. (**G**) Expression of key WNT pathway genes in OSBPL3 high- and low-expressing cell populations from the single-cell pancreatic cancer dataset GSE155698. (**H**) Violin plot showing the expression of WNT pathway-related immunosuppressive cytokines in macrophages, epithelial cells, and T cells with high or low OSBPL3 expression. (**I**) Cell-cell communication intensity across different cell subpopulations. Different colors represent signals emitted by various cell subpopulations. (**J**) Bubble plot depicting the expression of ligands generated by OSBPL3 high-expressing ductal cells across different cell subpopulations. (**K**) A schematic illustrating the role of high OSBPL3 expression in contributing to the immunosuppressive microenvironment in pancreatic cancer

of robust predictive biomarkers remains a pressing need [21]. In this study, we systematically constructed risk assessment and prognosis prediction models using multiple pancreatic cancer transcriptome datasets and identified key prognostic genes, including OSBPL3, that could serve as novel biomarkers for early diagnosis and therapeutic targeting [22]. Our models effectively distinguished pancreatic cancer patients from healthy controls, leveraging upregulated genes and a variety of machine learning algorithms to achieve optimal predictive performance. Compared to existing prediction models, which often face limitations such as suboptimal efficacy, narrow applicability, or outdated methodologies, our approach employed a broad combination of advanced machine-learning techniques and integrated risk and prognosis predictions [23]. This dual-model strategy not only enhanced predictive performance but also uncovered key genes linked to disease progression, such as ARNTL2 and OSBPL3, underscoring their potential roles in pancreatic cancer pathogenesis [23].

A key finding of our study is the association of OSBPL3 overexpression with an immunosuppressive tumor microenvironment (TME). Immune infiltration analyses revealed reduced infiltration of immune-killing cells, such as CD4 + and CD8 + T cells, and increased infiltration of immunosuppressive cells, including macrophages and Tregs, in patients with high OSBPL3 expression. This pattern was further validated through immunohistochemistry and cell-line experiments, as well as spatial transcriptomics, which confirmed the co-localization of OSBPL3 expression with markers of M2 macrophages and Tregs. These findings suggest that OSBPL3 may drive immune evasion by modulating the immune landscape of pancreatic cancer. Furthermore, single-cell analyses highlighted that OSBPL3 was highly expressed in tumor-associated Tregs and macrophages characterized by SPP1 or C1QC expression, particularly in late differentiation stages. Cell communication analysis demonstrated increased immunosuppressive signaling between OSBPL3-high tumor cells and T cells, as well as enhanced activation signals between tumor cells and fibroblasts. Importantly, the co-inhibitory TIGIT-PVR signaling axis was unique to the OSBPL3-high group, and PVR expression decreased upon OSBPL3 knockdown. These findings align with previous studies that identified TIGIT signaling as critical for CD8 + T cell exhaustion. The observed correlation between OSBPL3 expression and TIGIT-PVR signaling provides a mechanistic link to immune evasion and suggests potential therapeutic opportunities targeting this pathway, such as the anti-TIGIT antibodies currently in clinical trials [24]. Additionally, OSBPL3 appears to play a role in reprogramming the metabolic and signaling environment of pancreatic cancer. Pathway enrichment analysis of OSBPL3-high tumor subpopulations revealed significant activation of oncogenic pathways, including WNT, TGFβ, PI3K-AKT, and MAPK, which are known to be associated with resistance to immune checkpoint inhibitors [25]. Ligand-receptor pair analysis identified VCAN and SMAD3 as key targets in these pathways, further implicating OSBPL3 in driving immune suppression via inhibitory cell-cell communication.

Interestingly, the metabolic characteristics of the OSBPL3-high TME may contribute to its immunosuppressive nature. Immunosuppressive cells like Tregs and M2 macrophages predominantly rely on lipid oxidation rather than glycolysis, making them better adapted to high-lipid environments. This high-lipid TME, potentially driven by OSBPL3 overexpression, supports the survival and function of these cells while simultaneously promoting immunosuppression [26]. These observations align with prior studies demonstrating that lipid metabolism can modulate T cell function and exhaustion, particularly via pathways such as AKT-mTORC1-SREBP1 [27, 28]. Taken together, our findings highlight OSBPL3 as a critical mediator of the immunosuppressive TME in pancreatic cancer. By driving immune evasion through mechanisms such as enhanced TIGIT-PVR signaling, altered metabolic pathways, and recruitment of immunosuppressive cells, OSBPL3 contributes to poor responsiveness to immunotherapy. Furthermore, its involvement in key oncogenic signaling pathways

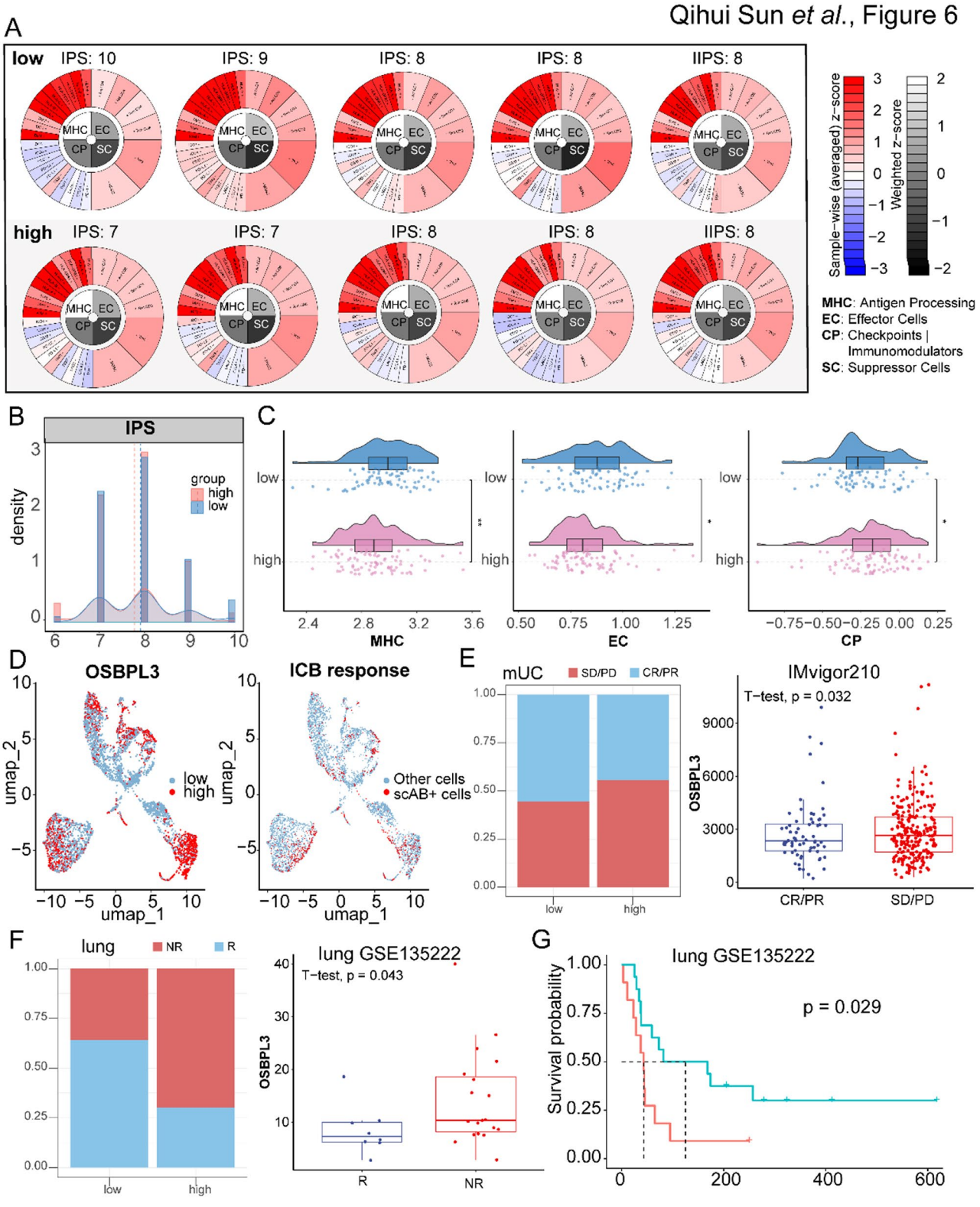

Fig. 6 (See legend on next page.)

(See figure on previous page.)

Fig. 6 High OSBPL3 Expression Predicts Poorer Response to Immunotherapy. (**A**) Z-scores of MHC, EC, CP, and SC in the top 5 samples with low and high OSBPL3 expression. (**B**) Density plot showing the distribution of Immunotherapy Prediction Score (IPS) values, derived from the integration of MHC, EC, CP, and SC scores, in pancreatic cancer samples with high and low OSBPL3 expression. (**C**) MHC, EC, and CP values in high- and low-expression OSBPL3 groups. Non-parametric tests were performed, with * indicating $P < 0.05$, ** indicating $P < 0.01$, and *** indicating $P < 0.001$. (**D**) Distribution of immune-positive cells (scAB + cells) and other cells in pancreatic cancer ductal cell subpopulations with high and low OSBPL3 expression, predicted by the scAB algorithm. (**E**) Proportion of CR/PR and SD/PD response groups in different OSBPL3 expression groups of mUC patients from the IMvigor210 dataset following immunotherapy. Expression of OSBPL3 in different immune therapy response groups of mUC patients from the IMvigor210 dataset. (**F**) Correlation between OSBPL3 expression and immune therapy response in the lung cancer immunotherapy dataset GSE135222. (**G**) Survival analysis of OSBPL3 expression in lung cancer patients after immunotherapy

suggests that OSBPL3 may also promote pancreatic cancer cell proliferation and progression.

Our study underscores the potential of OSBPL3 as a dual biomarker for risk assessment and prognosis prediction in pancreatic cancer. Moreover, OSBPL3 represents a promising therapeutic target for combination strategies aimed at overcoming immunotherapy resistance [29]. For instance, combining anti-TIGIT antibodies with inhibitors targeting lipid metabolism pathways or oncogenic signaling cascades may enhance immune activation and improve therapeutic efficacy [30]. Future studies should focus on further elucidating the mechanistic role of OSBPL3 in TME remodeling and exploring its therapeutic potential in preclinical and clinical settings. In particular, integrating OSBPL3-targeted therapies with existing immunotherapy regimens could open new avenues for improving outcomes in pancreatic cancer, a malignancy notoriously resistant to conventional treatments [31]. In conclusion, this study provides valuable insights into the role of OSBPL3 in shaping the immunosuppressive TME and highlights its potential as a therapeutic target to enhance immunotherapy efficacy. These findings contribute to our understanding of pancreatic cancer biology and offer new strategies for tackling this challenging disease.

Supplementary Information

The online version contains supplementary material available at https://doi.org/10.1186/s13062-025-00596-0.

Supplementary Material 1

Author contributions

Q.S., K.X., F.W., X.Z., Q.Z., Y.C., and T.W. designed all the experiments and wrote the manuscript, Q.S., Q.Z., X.Z., J.T., X.L. and Y.C. performed the experiments，and also collected and analyzed the data, Q.S., F.W., and K.X. contributed to the writing and editing of the manuscript and J.L. reviewed the manuscript before its submission. K.X. supervised the project and provided research funds and resources. All authors reviewed and approved the manuscript.

Funding

The work is partly supported by National Natural Science Foundation of China (#82072632 to K.X.) and Guangzhou Municipality Bureau of Science and Technology, Guangzhou, China (#202102010033 to K.X.) and Natural Science Foundation of Guangdong Province, China (#2022A1515012585 to K.X.).

Data availability

No datasets were generated or analysed during the current study.

Declarations

Ethical approval

The authors are accountable for all aspects of the work in ensuring that questions related to the accuracy or integrity of any part of the work are appropriately investigated and resolved. The study was conducted in accordance with the Declaration of Helsinki (as revised in 2013).

Reporting checklist

The authors have completed the TRIPOD reporting checklist.

Competing interests

The authors declare no competing interests.

Author details

[1]Center for Pancreatic Cancer Research, Department of Immunology, The South China University of Technology School of Medicine, Guangzhou, China
[2]Guangzhou Digestive Disease Center, The Second Affiliated Hospital, Guangzhou First People's Hospital, South China University of Technology School of Medicine, Guangzhou, China
[3]School of Medicine, South China University of Technology, Guangzhou 510006, China

Received: 10 December 2024 / Accepted: 6 January 2025
Published online: 09 January 2025

References

1. Qin C, Yang G, Yang J, et al. Metabolism of pancreatic cancer: paving the way to better anticancer strategies. Mol Cancer. 2020;19(1):50.
2. Halbrook CJ, Lyssiotis CA, Pasca di Magliano M, et al. Pancreatic cancer: advances and challenges. Cell. 2023;186(8):1729–54.
3. Siegel RL, Miller KD, Fuchs HE, et al. Cancer statistics, 2021. CA Cancer J Clin. 2021;71(1):7–33.
4. Klein AP. Pancreatic cancer epidemiology: understanding the role of lifestyle and inherited risk factors. Nat Rev Gastroenterol Hepatol. 2021;18(7):493–502.
5. Neoptolemos JP, Kleeff J, Michl P, et al. Therapeutic developments in pancreatic cancer: current and future perspectives. Nat Rev Gastroenterol Hepatol. 2018;15(6):333–48.
6. Maru SY, Jaffee EM. Pancreatic cancer is feeling the heat. J Immunother Cancer. 2024;12(10):e010124.
7. Ho WJ, Jaffee EM, Zheng L. The tumour microenvironment in pancreatic cancer — clinical challenges and opportunities. Nat Rev Clin Oncol. 2020;17(9):527–40.
8. Provenzano PP, Cuevas C, Chang AE, et al. Enzymatic targeting of the Stroma ablates physical barriers to treatment of pancreatic ductal adenocarcinoma. Cancer Cell. 2012;21(3):418–29.
9. Wu B, Zhang B, Li B, et al. Cold and hot tumors: from molecular mechanisms to targeted therapy. Signal Transduct Target Ther. 2024;9(1):274.
10. Amit M, Gil Z. Macrophages increase the resistance of pancreatic adenocarcinoma cells to gemcitabine by upregulating cytidine deaminase. Oncoimmunology. 2013;2(12):e27231.
11. B J R, C STSQM. Safety and activity of Anti–PD-L1 antibody in patients with Advanced Cancer. N Engl J Med. 2024;366(26):2455–65.
12. Gulyás G, Sohn M, Kim YJ, et al. ORP3 phosphorylation regulates phosphatidylinositol 4-phosphate and Ca2 + dynamics at plasma membrane–ER contact sites. J Cell Sci. 2020;133(6):jcs237388.

13. Gregorio-King CC, Collier GR, McMillan JS, et al. ORP-3, a human oxysterol-binding protein gene differentially expressed in hematopoietic cells. Blood. 2001;98(7):2279–81.
14. Yan D, Lehto M, Rasilainen L, et al. Oxysterol binding protein induces Upregulation of SREBP-1c and enhances hepatic lipogenesis. Arterioscler Thromb Vasc Biol. 2007;27(5):1108–14.
15. Zhong W, Lin W, Yang Y, et al. An acquired phosphatidylinositol 4-phosphate transport initiates T-cell deterioration and leukemogenesis. Nat Commun. 2022;13(1):4390.
16. Aibara D, Sakaguchi A, Matsusue K. Oxysterol-binding protein-like 3 is a novel target gene of peroxisome proliferator-activated receptor γ in fatty liver disease. Mol Cell Endocrinol. 2023;565:111887.
17. Hao N, Zhou Y, Li Y et al. Clinical Value and Potential Mechanisms of Oxysterol-Binding Protein Like 3 (OSBPL3) in Human Tumors. In: Frontiers in Molecular Biosciences. 2021.
18. Stein S, Lemos V, Xu P, et al. Impaired SUMOylation of nuclear receptor LRH-1 promotes nonalcoholic fatty liver disease. J Clin Invest. 2017;127(2):583–92.
19. Li Y, Zheng Y, Huang J et al. CAF-macrophage crosstalk in tumour microenvironments governs the response to immune checkpoint blockade in gastric cancer peritoneal metastases. Gut, 2024: gutjnl-2024-333617.
20. Curcio C, Mucciolo G, Roux C, et al. PI3Kγ inhibition combined with DNA vaccination unleashes a B-cell-dependent antitumor immunity that hampers pancreatic cancer. J Exp Clin Cancer Res. 2024;43(1):157.
21. Liu H, Zhang W, Zhang Y, et al. Mime: a flexible machine-learning framework to construct and visualize models for clinical characteristics prediction and feature selection. Comput Struct Biotechnol J. 2024;23:2798–810.
22. Wu M, Li X, Zhang T et al. Identification of a Nine-Gene Signature and establishment of a Prognostic Nomogram Predicting overall survival of pancreatic Cancer. Front Oncol, 2019, 9.
23. Hu Q, Masuda T, Koike K, et al. Oxysterol binding protein-like 3 (OSBPL3) is a novel driver gene that promotes tumor growth in part through R-Ras/Akt signaling in gastric cancer. Sci Rep. 2021;11(1):19178.
24. Park JK, Jeong Hoh, Kim H, et al. Single-cell transcriptome analysis reveals subtype-specific clonal evolution and microenvironmental changes in liver metastasis of pancreatic adenocarcinoma and their clinical implications. Mol Cancer. 2024;23(1):87.
25. Wang S, Lai JC, Li Y et al. Loss of CDKN2A enhances the efficacy of Immunotherapy in EGFR Mutant Non-small Cell Lung Cancer. Cancer Res, 2024.
26. Gabitova-Cornell L, Surumbayeva A, Peri S, et al. Cholesterol Pathway Inhibition Induces TGF-β Signaling to Promote Basal Differentiation in Pancreatic Cancer.Cancer Cell. 2020;38(4):567–583.e11.
27. Tian K, Ying Y, Huang J, et al. The expression, immune infiltration, prognosis, and experimental validation of OSBPL family genes in liver cancer. BMC Cancer. 2023;23(1):244.
28. Cheng C, Geng F, Cheng X, et al. Lipid metabolism reprogramming and its potential targets in cancer. Cancer Commun. 2018;38(1):27.
29. Chou CW, Hsieh YH, Ku SC, et al. Potential prognostic biomarkers of OSBPL Family genes in patients with pancreatic ductal adenocarcinoma. In: Biomedicines; 2021.
30. Ostroumov D, Duong S, Wingerath J et al. Transcriptome profiling identifies TIGIT as a marker of T-Cell exhaustion in Liver Cancer. Hepatology, 2021, 73(4).
31. Cho BC, Abreu DR, Hussein M, et al. Tiragolumab plus Atezolizumab versus placebo plus atezolizumab as a first-line treatment for PD-L1-selected non-small-cell lung cancer (CITYSCAPE): primary and follow-up analyses of a randomised, double-blind, phase 2 study. Lancet Oncol. 2022;23(6):781–92.

Publisher's note